Taking a look at both sides of the ice: comparison of ice thickness and drift speed as observed from moored, airborne and shore-based instruments near Barrow, Alaska

Andrew R. Mahoney[1], Hajo Eicken[1], Yasushi Fukamachi[2], Kay I. Ohshima[2], Daisuke Simizu[3], Chandra Kambhamettu[4], Rohith MV[4], Stefan Hendricks[5], Joshua Jones[1]

[1] Geophysical Institute, University of Alaska Fairbanks, Fairbanks, Alaska
[2] Institute of Low Temperature Science, Hokkaido University, Sapporo, Japan
[3]National Institute of Polar Research, Tachikawa, Japan
[4] University of Delaware
[5] Alfred Wegener Institute

Abstract

Data from the Seasonal Ice Zone Observing Network (SIZONet) acquired near Barrow, Alaska during the 2009-10 ice season allow novel comparisons between measurements of ice thickness and velocity. Data from an airborne electromagnetic (AEM) survey that passed over a moored ice profiling sonar (IPS) provide independent measurements of total ice and snow thickness and ice draft at a scale of 10 km. Once differences in sampling footprint size are accounted for, we reconcile the respective probability distributions and estimate the thickness of level sea ice to be 1.48 ± 0.1 m with a snow depth of 0.12 ± 0.07 m. We also complete what we believe is the first independent validation of radar-derived ice velocities by comparing measurements from a coastal radar with those from an under-ice Acoustic Doppler Current Profiler (ADCP). After applying a median filter to reduce high frequency scatter in the radar-derived data, we find good agreement with the ADCP bottom-tracked ice velocities. With increasing regulatory and operational needs for sea ice data, including the number and thickness of pressure ridges, coordinated observing networks such as SIZONet can provide the means of reducing uncertainties inherent in individual datasets.

Introduction

With ongoing retreat and thinning of Arctic sea ice (Stroeve and others, 2012, Wang & Overland, 2012) and growing commercial interest in resource extraction and marine navigation (Schmidt, 2011, Arctic Council, 2009), there is an increasing demand for observational data of ice thickness and velocity. Although a growing number of pan-Arctic and regional sea ice thickness datasets are becoming publically available (e.g., Laxon and others, 2013, Kurtz and others, 2009), their usefulness for regulatory and operational purposes is limited by spatial resolution and error characteristics. Altimetry-derived ice thicknesses suffer from large errors, primarily due to uncertainties in the snow depth and the densities of the sea ice and snow. Kwok and Cunningham (2008) estimate that the uncertainties in densities alone account for 10-20% of the variance in Arctic sea ice thickness calculated using Ice Cloud and land Elevation Satellite (ICESat) data. Moreover, the spatial resolution of these satellite-derived products is too coarse to resolve pressure ridges, which comprise the thickest elements of the ice cover.

Airborne and submarine platforms provide the best means of obtaining sea ice thickness data at intermediate spatial scales that sample enough ice to obtain useful thickness statistics while also resolving individual ridges. Airborne thickness surveys use altimetric techniques similar to those used from space or they employ a combination of altimetry and electromagnetic induction (Haas and others, 2010, Haas and others, 2009) to calculate total snow and ice thickness without requiring knowledge of their densities. Upward looking sonar on naval submarines travelling beneath the ice have provided a wealth of data on sea ice thicknesses dating back to the early 1970s (Thorndike and others, 1975), but in recent years it has become more common to use moored ice profiling sonars (IPSs) to observe the ice as it passes overhead (e.g., Melling and others, 1995). Submarine methods also use a form of altimetry to determine ice thickness, but instead of measuring freeboard they measure the draft of ice and are therefore less sensitive to uncertainties in density.

The measurement of ice velocity is essential for a proper analysis of ice thickness data collected by IPSs and it is common practice to deploy Acoustic Doppler Current Profilers (ADCPs) alongside each IPS to measure the drift of ice. Ice velocity is also a key constraint, together with ice thickness, for the design of Arctic offshore structures (ISO, 2010). Observing ice motion may be either Eulerian (as in the case of a mooring measuring ice drift at a fixed point), or Lagrangian (such as using a GPS-tracked buoy to record the path of an ice floe). Here, we focus on Eulerian measurements of ice velocity, which can also be derived at a grid of points using sequences of images of sea ice (e.g., Fowler, 2003, Kwok & Cunningham, 2003).

In this paper, we combine data collected as part of the Seasonal Ice Zone Observing Network (SIZONet; sizonet.org) to make novel comparisons between coincident and colocated observations of sea ice from above and below. Using airborne electromagnetic (AEM) data collected along a flight that passed over a moored IPS, we compare two completely independent measurements of the local ice thickness distribution around the mooring. This comparison also allows us to estimate the thickness of the snow on top of the ice. We also make a comparison between ice velocities recorded by an upward looking ADCP and those determined from sequences of imagery acquired by a coastal based radar system. To our knowledge, this is first such validation of surface radar-derived ice velocities and it demonstrates the suitability of such systems for real time ice and hazard monitoring in the Arctic coastal regions.

Datasets and methods

Ice draft and velocity measurements from under-ice moorings

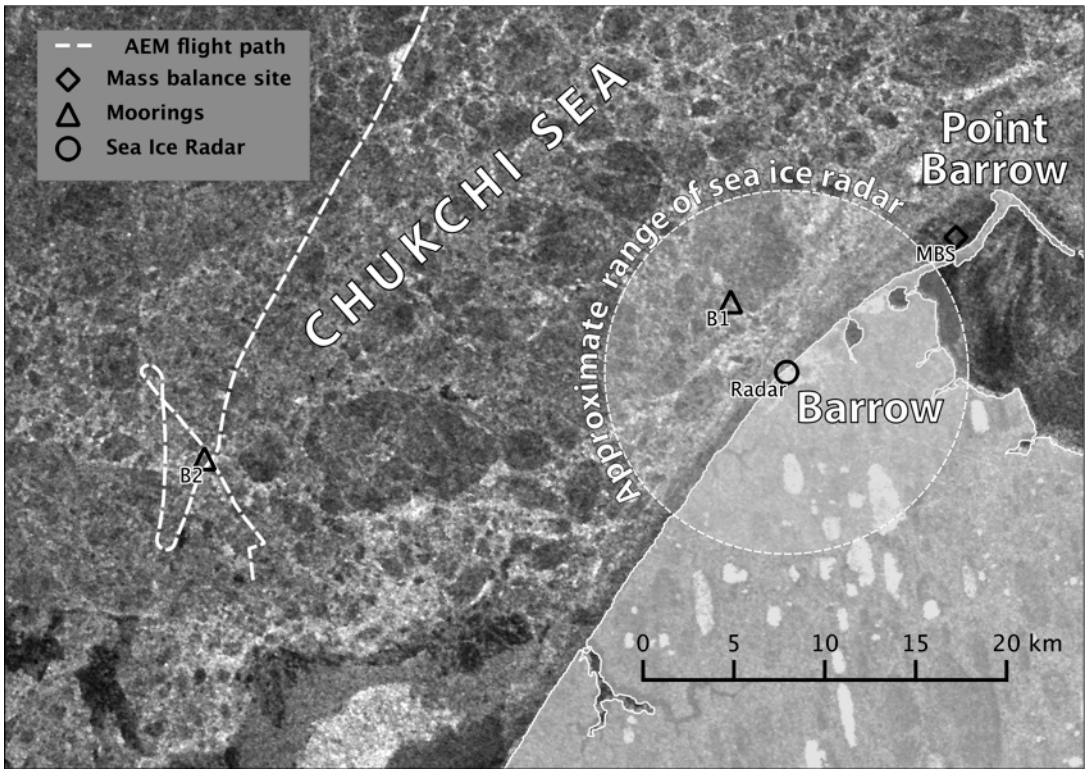

Figure 1: AEM flightpath over mooring B2 on April 12, 2010 near Barrow, Alaska. Also shown are the locations of mooring B1, an ice mass balance site (MBS) and the approximate range of a coastal sea ice radar system installed on a building in Barrow. The background is an Envisat ASAR image acquired 1 hour after the AEM flight passed over mooring B2.

Figure 1 shows the location of two moorings (B1 and B2) deployed near Barrow as part of SIZONet. Mooring B1 was deployed at 71.32698° N, 156.87663° W and mooring B2 was deployed at 71.23471° N, 157.65271° W. These moorings each comprised an IPS and ADCP as well as conductivity-temperature (C-T) and temperature-pressure (T-P) recorders (Figure 2). The IPSs are used to measure the draft of the sea ice passing overhead while the ADCPs measure current velocity profile of the overlying water column and, of particular relevance here, the velocity of the ice through bottom tracking.

The calculation of ice draft from raw IPS data is an involved process, described in detail by Melling et al. (1995). In brief, the distance from the sonar to the ice or open water surface is determined from the travel time of echoes, with adjustments made for instrument tilt. Corrections for sound speed variations over time are made by identifying periods when open water was above the sonar and reconciling the measured echo travel time with the depth determined from an onboard pressure sensor. Through this approach, the draft of the level ice can be measured to an estimated accuracy and precision of ±0.05 m (Fukamachi and others, 2006). Ice draft measurements are made at 1-second intervals.

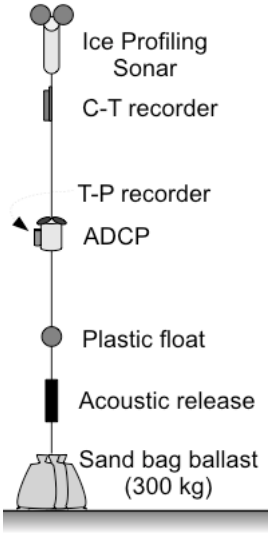

Figure 2: Configuration of SIZONet moorings deployed near Barrow, Alaska in 2009-10.

A moored IPS generates a time series of ice draft at a fixed location as the sea ice drifts overhead. Since the drift velocity of the ice is not constant over time, these data cannot be used to derive distance-referenced probability distributions. It is therefore necessary to transform the time series into a pseudo-spatial series using ice velocity data. In our case we use ice velocities calculated from the ADCP bottom track data. The ice velocity is determined from the Doppler shifts of acoustic signals returned from the bottom of the ice. This is similar to the method used to determine the water velocity, but a separate longer-pulse signal is used to achieve accuracies of a few mm/s (Gordon, 1996).

The bottom track data are recorded every 15 minutes and so must be interpolated to match the 1-second timeseries recorded by the IPS. Each interpolated velocity measurement thus represents an effective sampling distance for each ice draft measurement. We then use a cubic spline interpolation to create a regularly spaced pseudo spatial series of ice draft with 1m spacing, approximately matching the footprint of the sonar beam on the underside of the ice (Williams and others, 2008). The measurement of ice draft can be related to ice thickness by invoking Archimedes principle, with the total weight of the ice and snow equal to the weight of the water displaced. If we assume that the ice at each measurement is in isostatic equilibrium, then this can be expressed as:

$$\rho_i Z_i + \rho_s Z_s = \rho_w D \qquad (1)$$

where ρ_i, ρ_s and ρ_w are the densities of ice, snow and water, respectively. Z_i and Z_s are the thicknesses of ice and snow, respectively, and D is the ice draft.

Airborne Electromagnetic (AEM) ice thickness measurements

AEM sounding uses electromagnetic induction to determine the distance from the towed instrument, known as an EM-bird, to the water surface(Haas and others, 2010, Haas and others, 2009). The technique involves emitting a primary EM field (in this case at 4.09 kHz), which induces a secondary field in the conductive seawater. Using a 1-D model in which the seawater and sea ice conductivities are

specified (Pfaffling and others, 2007), the distance to the underside of the ice can be determined from the relative strength of the in-phase component of the secondary field. At the same time, the distance to the upper surface of the ice (or snow if present) is measured using a laser altimeter mounted in the EM-bird. The combined thickness of snow and sea ice is determined by subtracting these two distances (Figure 3). In comparison with field measurements, this technique is found to have an accuracy of better than 0.1 m over level ice (Haas and others, 2009).

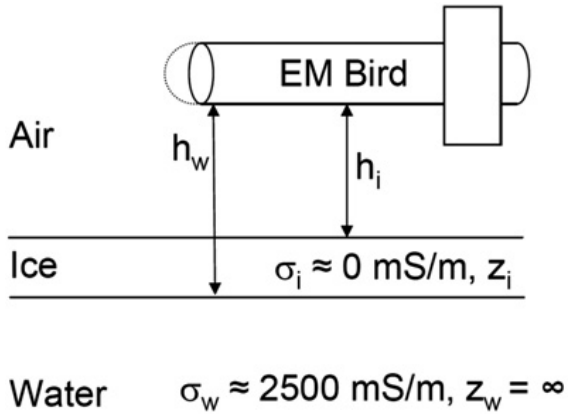

Figure 3: From Haas *et al.*[2009]. Principle of AEM thickness sounding, using a bird with transmitter and receiver coils and a laser altimeter. Ice thickness Z_i is obtained from the difference of measurements of the bird's height above the water and ice surface, h_w and h_i, respectively.

In April 2010, two AEM flights were made over the sea ice near Barrow, Alaska, as part of SIZONet activities. Figure 1 shows part of the flight path on April 12, 2010, during which two passes were made over mooring B2. A helicopter was used for these flights, allowing us to make controlled, tight turns over the mooring location. The EM-bird was flown at an altitude of approximately 15m, giving an effective sampling footprint of approximately 70m. Each AEM measurement is thus a mean value of ice and snow thickness over this area. The EM-bird will therefore tend to under estimate the maximum thickness of ice ridges, though it can be expected to give an accurate measure of the overall ice volume (Pfaffling and others, 2007).

Gridded ice velocities from coastal sea ice radar data

The University of Alaska Fairbanks (UAF) has operated a coastal sea ice radar discontinuously since the 1970s (Shapiro & Metzner, 1989, Mahoney and others, 2007, Druckenmiller and others, 2009, Mv and others, 2013, Jones, 2013). Data from the current system are available in near real time from http://seaice.alaska.edu/gi/observatories /barrow_radar. Figure 4 shows an image from the radar on April 12, 2010 coinciding with the Envisat ASAR image shown in Figure 1. The coastal radar has a considerably lower grazing angle than space-based systems and is reliant on rough surfaces with higher local incidence angles to act as natural reflectors. The coastal radar is therefore mostly sensitive to ridges and floe edges, with little or no energy returned from areas of level ice in between. As a result, images from the coastal radar often contain “empty” regions without features that can be tracked through commonly used techniques based upon cross-

correlation of image pairs. To overcome these challenges, we use a combination of dense and sparse optical flow methods to generate gridded ice velocities (Mv and others, 2013)

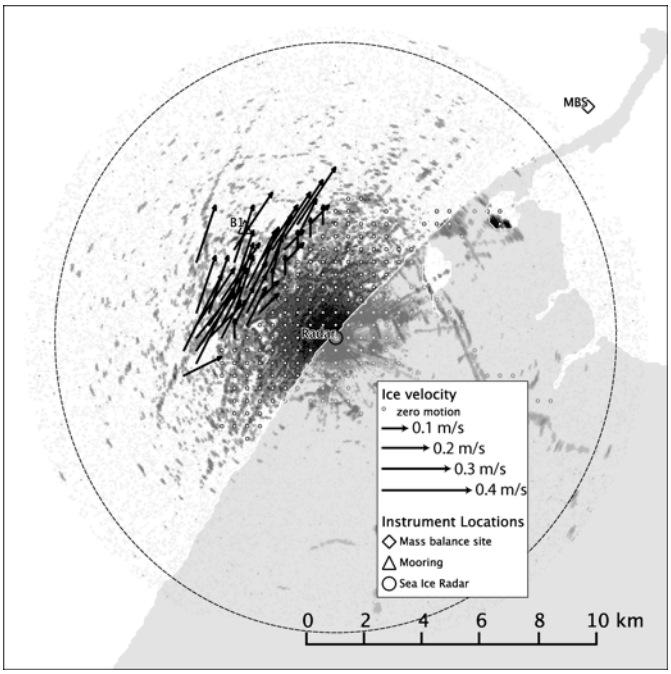

Figure 4: Coastal radar image acquired at 21:25, April 12 2010 (UTC) coincident with the Radarsat image in Figure 1. Vectors show ice velocities determined from consecutive images.

The radar data are recorded in range-azimuth space with 512 samples per range line and up to 4096 lines per rotation. The calculation of velocity in physical units requires accurate geolocation of the radar imagery. We determined the correct range resolution and orientation of the imagery using linear ground control features such as pipelines, roads and snow fences that were recognizable in both the radar imagery and high resolution satellite data available through the Geographic Information Network of Alaska (GINA). At a nominal range setting of 6 nautical miles, we determined the range resolution to be 21.5 ± 0.5 m, which is the pixel size chosen for reprojection of the data to a Cartesian plane. The radar system records images every 120 rotations, which at a rotation speed of ~0.5 Hz corresponds to approximately 4 minutes between images although this interval is variable due to small changes in rotation speed of the radar antenna. Since the file creation times for each radar image are only preserved to an accuracy of one minute, it is therefore difficult to precisely determine the time interval over which motion is observed. However, over the whole record for the 2009-10 season, we calculate an average interval between consecutive images of 231 ± 9 s. Together, these uncertainties in spatial scale and time interval amount to a 5% error in the radar-derived velocities.

The velocity vectors shown in Figure 4 are calculated on a 20 x 20 pixel (438 x 438 m) grid and have been median-filtered in time to remove erroneous values (this procedure is discussed in more detail in the results section below). Grid points with zero velocity are shown by white dots and indicate the extent of landfast ice at the time of data acquisition. Grid points where no velocity measurement could be

determined are blank. Velocity determination typically fails due to one of three causes: i) a lack of reflectors; ii) excessive ice motion; or iii) rapid changes in reflector orientation or shape due to ice movement or deformation. For the purposes of comparing radar-derived ice velocities with the bottom track data recorded by the ADCP, we calculate the mean velocity recorded at the four grid points surrounding mooring B1.

Results

Ice thickness over mooring B2

Figure 5 shows the path of the AEM flight on April 12, 2010 (in white) over mooring B2 together with a pseudo track of ice motion (in gray) derived by integrating the bottom track velocity recorded by the ADCP forward and backwards in time from the time of the AEM overpass. The continuous white lines indicate portions of the flight made at measurement altitude within a 10 km radius of the mooring (shown by the black dashed circle). The white dots indicate the calculated 6-hourly positions along the pseudo track. The helicopter made two separate overpasses, which are indicated by the labeled arrows. Table 1 lists the time and distance of the closest point on each overpass together with the AEM-derived ice thickness and the IPS-measured ice draft at the times. The background is the Envisat SAR image shown in Figure 1, which was acquired at 21:26:59 UTC on April 12, just one hour after the first overpass. The black cross indicates the location of ice that was at the mooring at the time of overpass 1, based on the pseudotrack data.

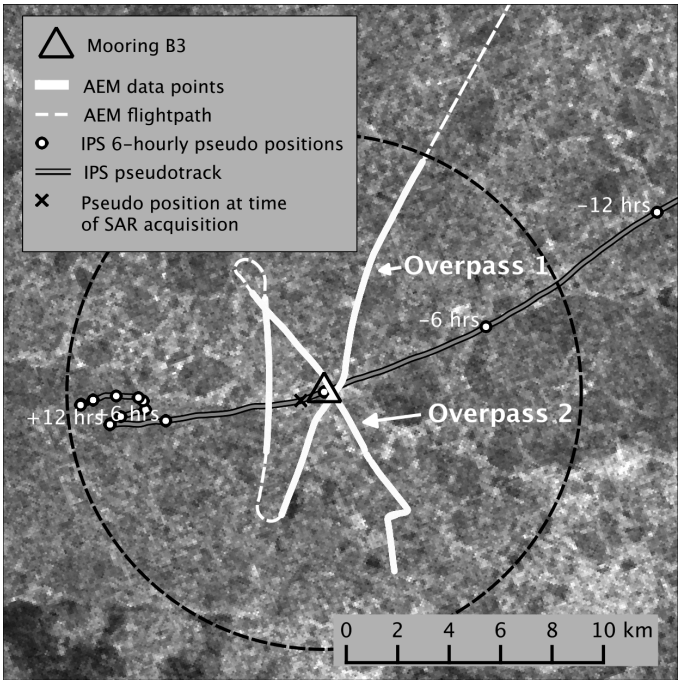

Figure 5: Map showing the AEM flightpath over mooring B2. The gray line indicates a pseudotrack of ice drift calculating by integrating the bottom track velocity over time. White dots indicate the 6-hourly pseudo positions of the ice before and after the overpass. Only those at ± 6 and 12 hours are labeled to reduce clutter in the figure. The black cross indicates ice that was at the mooring at the time of overpass 1.

Table 1: Time, closest distance and coincident measurements for overpasses 1 and 2

Overpass	*Time (UTC)*	*Spatial offset*	*Ice + snow thickness*	*Ice draft*
1	20:26:50	345 m	1.54 m	4.93 m
2	20:38:05	269 m	1.96 m	3.99 m

Table 1 shows significant differences between the coincident AEM and IPS measurements at the time of each overpass. In both cases the IPS-measured draft is greater than the AEM-measured combined snow and ice thickness. In some cases such differences can be accounted for by the larger sampling footprint of the EM-bird, if there happened to a narrow ridge keel above the IPS at the time of the overpass, the thickness of which would be underestimated in the AEM data. However, examination of the IPS before and after each overpass indicates this is not the case. Instead, it is more likely the difference is due to the spatial offset between the actual measurement locations. This is supported by the SAR image in Figure 5, which shows high backscatter in the region of the mooring at the time of the overpass (marked by black cross) indicating rough, heterogeneous ice.

Neither of the two overpasses was aligned with the drift of ice at the time, which means it is not feasible to attempt to colocate the measurements more accurately. We therefore compare AEM and IPS measurements by calculating their probability distributions using all data that falls within 10 km of mooring B2 (indicated by the black dashed circle in Figure 5). Figure 6 shows the distributions of AEM-derived ice and snow thickness and IPS-derived ice draft, binned into 0.05m intervals. Both distributions have pronounced modes, which represent the thickness and draft of level undeformed ice. The AEM data indicate a modal combined thickness of ice and snow of 1.6 ± 0.025 m while the IPS data show a modal ice draft of 1.35 ± 0.025 m. These values and their relationship with density and snow depth are discussed in more detail in the following section.

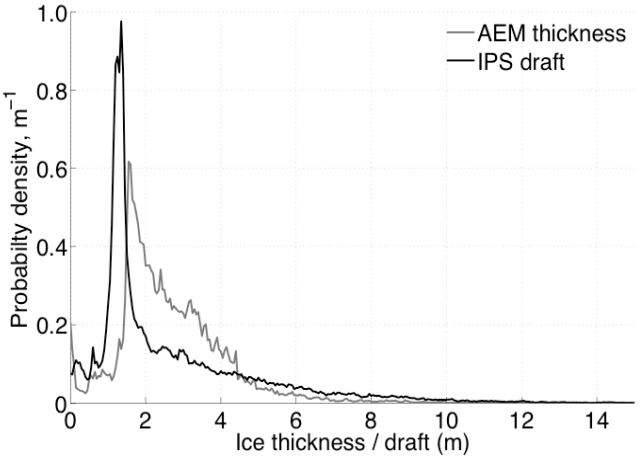

Figure 6: Probability distribution of combined ice and snow thickness (AEM) and ice draft (IPS) derived from all measurements within 10 km of mooring B2.

Ice velocities near Barrow during 2009-10 winter season

Figure 7 shows a comparison of ice velocities at the B1 mooring location over the winter season of 2009-10 derived from the ice radar and ADCP bottom track

data. For this comparison, we binned the radar-derived values every 15 minutes to match the sampling interval of the ADCP. We have also excluded data from periods with a significant open water fraction and when the instrument tilt exceeded 20 degrees. The presence of open water can be inferred from increased magnitude and variability of the bottom track error recorded by the ADCP due to the presence of surface waves (Belliveau and others, 1990). We applied a 2-hour running mean to the bottom track error values and discarded data from periods with error values greater than 0.1 m s^{-1}.

The radar-derived velocities show significant scatter and a tendency for the optical flow algorithm to overestimate ice motion in comparison with bottom track ice velocities. However, we see considerably better agreement when we apply a 2-hour running median filter to the radar-derived data, with tighter clustering around the line y=x and an improvement in the RMS difference in velocity magnitudes from 0.24 m s^{-1} to 0.12 m s^{-1}. The close agreement in both alongshore and offshore components indicates that both datasets are well aligned geographically.

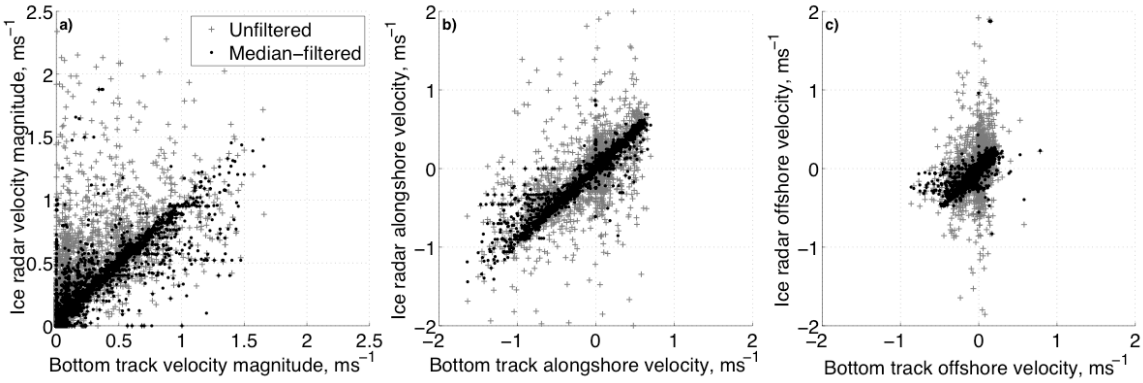

Figure 7: Scatter plots comparing ADCP- and radar-derived ice velocities for winter season of 2009-10.

Figure 8 shows timeseries of the median-filtered radar-derived ice velocities ADCP bottom track velocities from November 1, 2009 to June 30, 2010. These plots confirm the overall good agreement between the two independently derived ice velocities and they allow closer scrutiny of those occasions when the results differ. The grey boxes indicate periods of open water inferred from the bottom track error as described above. It is clear that these periods correspond to the fastest velocities and also coincide with many of the gaps in the coastal radar velocity record. Examination of the radar imagery during these data gaps reveals an absence of a lack of reflectors over the mooring site. We remind the reader that, due to the insensitivity of the coastal radar system to areas of smooth ice, the absence of reflectors in the imagery does not necessarily imply an absence of ice on the ocean, but in those cases where there is sufficient daylight we are able to confirm the presence of open water through examination of images from the Barrow sea ice webcam (http://seaice.alaska.edu/gi/observatories/barrow_webcam), which is colocated with the radar. Despite the gaps in the radar velocity record, there are occasions when the radar detected and tracked ice during periods of inferred open water. For these cases the overall RMS difference between the bottom track data

and median-filtered radar-derived ice velocity is 0.48 m s^{-1}, with a tendency for the radar to underestimate the ice velocity relative to the ADCP.

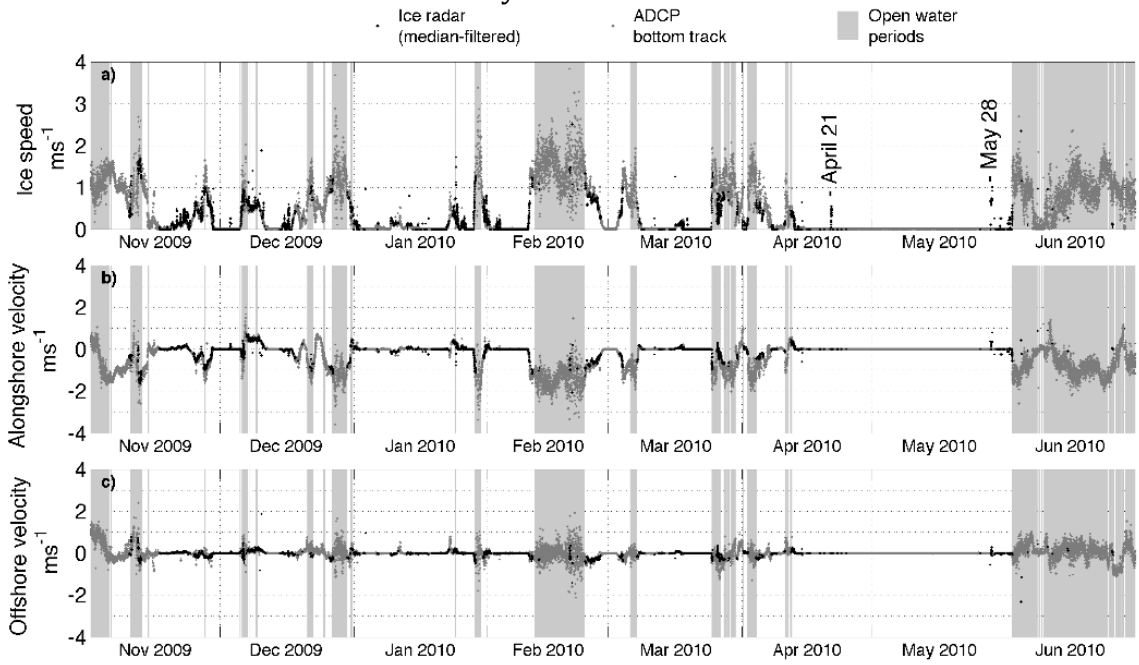

Figure 8: Timeseries of (a) ice velocity magnitude and (b) alongshore and (c) offshore components derived from the ice radar and ADCP bottom track data.

Discussion

Reconciling thickness and draft measurements

To our knowledge, the AEM flight over mooring B2 allowed the first direct comparison between airborne and submarine measurements of ice thickness at a scale larger than a few hundred meters. To compare AEM and IPS data it is important to understand the measurements that each instrument makes and how these relate to each other. Primarily it is important to recall that the EM-bird measures the combined thickness of snow and ice while the IPS measures just the draft of the ice. Rearranging equation (1) and substituting a thickness-weighted mean density of snow and ice, ρ^*, we can express the expected relationship between the AEM and IPS measurements as:

$$\left(Z_i + Z_s\right) = \frac{\rho_w}{\rho^*} D \qquad (2)$$

where

$$\rho^* = \frac{\rho_i Z_i + \rho_s Z_s}{Z_i + Z_s} \qquad (3)$$

At the time of the AEM overpass, the temperature and salinity at mooring B2 were -1.686 °C and 31.69, respectively, which yields a seawater density, ρ_w, of 1025 kg m^{-3}. Substituting this and the modal values derived from Figure 6 (Z_i+Z_s = 1.6 ± 0.025 m and D=1.35 ± 0.025 m), we derive a value of ρ^* of 860 ±30 kg m^{-3}. Assuming a sea ice density of 910 ±20 kg m^{-3} (Timco & Frederking, 1996) and a snow density

of 300 ±100 kg m^{-3}, taken from data for the month of March reported by Warren *et al.* (1999), we can use equation (3) to estimate that the level ice in the vicinity of mooring B2 on April 12, 2010 was 1.48 ± 0.09 m thick with a snow depth of 0.12 ± 0.09 m. Here, we have assumed the uncertainties are normally distributed and uncorrelated and we used the Gaussian method to propagate errors. Although the largest uncertainty, both in relative and absolute terms, is that for snow depth, the uncertainty in the value of ρ^* has the biggest effect on the derived values. This in turn is dependent on the uncertainties in the densities of water and ice and our ability to determine the modes in the AEM and IPS data.

For comparison, ice thickness at the UAF mass balance site (Figure 1) on April 12 was 1.24 m and the mean snow depth was 0.35 m. Although these values are not in agreement, it is natural to expect sea ice to be thinner underneath a thicker snow cover. Moreover, although measurements of snow on drifting sea ice are rare, we expect snow to be thicker on landfast ice along the Alaska Chukchi coast than on drifting ice offshore. Shorefast ice typically forms earlier, collecting more snow including snow drifting in from the tundra, whereas the prevailing northeasterly winds create a semi-persistent coastal polynya near Barrow (Mahoney and others, 2012, Eicken and others, 2006) that may reduce the amount of snow advected onto drifting sea ice downwind.

Closer examination of the two distributions in Figure 6 shows that they differ not only in the position of their modes, but also in the shape of the tail, most noticeably for ice thicknesses less than 4 m. This difference cannot be accounted for by a simple isostatic assumption, so instead we consider the differing footprints of the two instruments. To better match the footprints of the two instruments, we applied a 70 m boxcar smoothing filter to the IPS data. Figure 9 shows that smoothing the IPS data changes the shape of the tail of its distribution to more closely resemble that of the AEM data. A Gaussian filter was also tried, but resulted in a poorer fit. Having reconciled the sampling footprints of the IPS and AEM, we then applied a stretching to the smoothed IPS draft distribution that minimized the RMS difference between it and the AEM distribution. Using this approach we find a conversion factor from ice draft to total thickness of 1.20 ± 0.01 m (Figure 10), which corresponds to distribution-wide mean value of ρ^* of 850 ± 0.30 kg m^{-3}. Within 10 km of mooring B2, the mean thickness of ice and snow measured by the EM-bird is 2.66 m. Our mean value ρ^* therefore corresponds to a mean ice thickness of 2.40 ±0.14 m and a mean snow depth of 0.26 ±0.14 m.

Although Figure 10 shows good agreement between the modes of the AEM and smoothed, shifted IPS, there are differences in the two distributions that warrant further comment. We expect the distributions to differ simply because the AEM flight path and IPS pseudotrack do not overlap and the two sensors did not observe exactly the same ice. We believe this explains why the AEM data show a greater amount of thin ice <1 m than the IPS data. There are also differences in the tail such that the AEM data indicate more ice between 1.4 m and 4.0 m and less ice > 4 m than the IPS data. This may derive from the different sampling areas, but it also probably indicates that deformed ice must be treated differently than level ice when it comes to assumptions concerning the effective mean ice density or electrical conductivity. This is discussed further in the conclusions. The relative over- and under-

observation of ice thinner and thicker than ~4 m, respectively, might also be explained if the sensitivity of the EM-bird was reduced to the noise level of the receiver at this equivalent range. However, theoretical considerations of the EM response show that signal-to-noise ratios are not critical until a range of 30-35m, corresponding to an ice thickness of 15-20 m at a survey altitude of 15m.

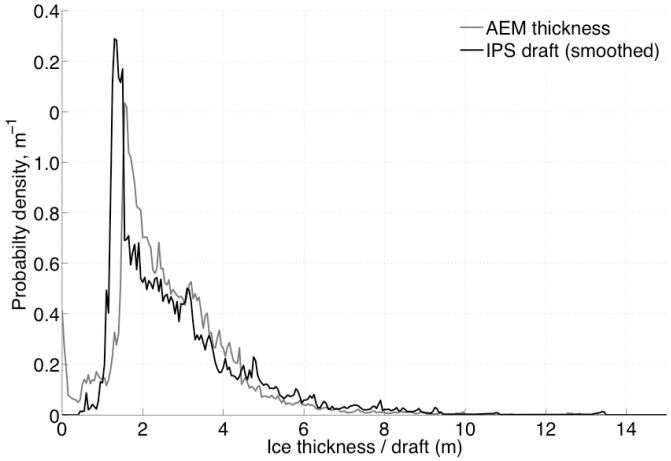

Figure 9: Probability distribution of combined ice and snow thickness (AEM) and smoothed ice draft (IPS) derived from all measurements within 10 km of mooring B2.

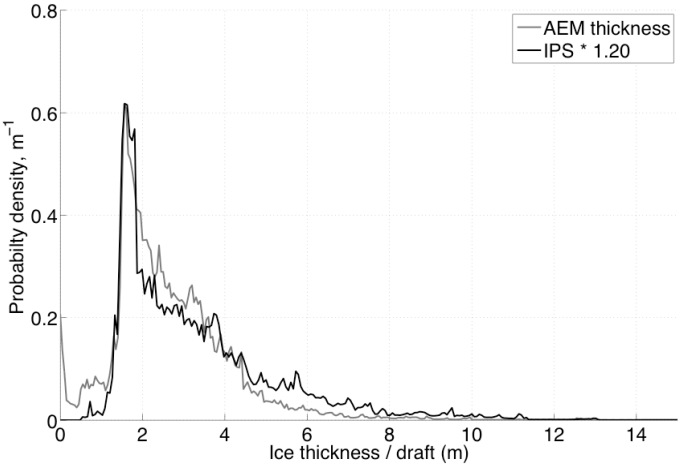

Figure 10: Probability distribution of combined ice and snow thickness (AEM) and smoothed ice draft (IPS) derived from all measurements within 10 km of mooring B2.

Coastal ice motion observed from above and below

Figure 8 shows the variability of ice motion at one point in the coastal zone near Barrow over a full ice season. Periods of zero ice motion indicate times when the ice above the mooring was landfast. The record shows landfast ice forming over the mooring as early as mid-November with several attachment and detachment events occurring throughout the year. In general, the periods of landfast ice become longer over the course of the year before final break up over the mooring around the beginning of June. Both the ADCP and the coastal radar system identify the beginning and end of these landfast periods, though in some cases the period of zero

motion coincides with data gaps in the radar-derived ice velocity record (e.g. the latter part of April and most of May). Examination of the radar imagery on these occasions indicates these gaps are due to a lack of reflectors over the mooring. However, the presence of ice can be confirmed from the presence of stationary reflectors in the surrounding neighborhood. On other occasions, the radar data show apparent ice motion while the ADCP data continues to indicate landfast ice (e.g April 21 and May 28). In these cases we find that the ice motion algorithm was confused by the passage of snow squalls and migrating birds.

In identifying the onset of ice motion at the end of landfast periods, the ADCP and radar-derived ice velocity records provide accurate timings of detachment events. The detachment of landfast ice represents a significant hazard to anyone on the ice when it begins to move. At the same time, such events are important to communities along the Alaska Chukchi coast during the spring whaling season, since any open water created provides access to hunt the whales migrating north along coast (Druckenmiller and others, 2010, George and others, 2004). Previous studies of coastal ice dynamics using surface radars have noted that it may be possible to detect precursor events leading up to detachments. Shapiro and Metzner (1989) and Mahoney *et al.* (2007) report the occurrence of "flickering" in the radar imagery prior to breakout events. MV *et al.* (2013) have taken this further to develop an algorithm based on Hidden Markov Models that has successfully detected some breakout events based on "hidden" characteristics of the gridded flow field. For a more detailed study of landfast ice detachments, including an analysis of ice deformation from radar-derived gridded ice velocities, see Jones (2013).

Conclusions

By assembling a range of SIZONet datasets acquired in the 2009-10 ice season near Barrow, Alaska, we have been able perform unique comparisons between coincident measurements of sea ice from above and below. Once differences in sampling footprint size between the EM-bird and the IPS had been accounted for, the probability distributions of ice thickness and draft within 10 km of mooring B2 on April 12, 2010 could be reconciled by a assuming mean density of the combined snow and ice cover. Moreover, this value can be used to estimate the relative proportions of snow and ice comprising the thickness measured by the EM-bird. Assuming sea ice and snow densities of 0.91 ± 0.02 g cm^{-3} and 0.3 ± 0.1 g cm^{-3}, respectively, we estimate the thickness of level sea ice near mooring B2 to be 1.48 ± 0.09 m with a snow depth of 0.12 ± 0.09 m. Applying this method to the whole thickness distribution, including thick deformed ice, we estimate a mean ice thickness and snow depth of 2.40 ± 0.14 m and 0.26 ± 0.14 m, respectively. However, by including deformed ice in the latter calculation, we may be overestimating the effective mean density of the ice, which in turn will lead to an underestimation of ice thickness and an overestimation of snow depth.

The inhomogeneous composition of deformed ice creates significant uncertainty in the thickness of ridges derived from both IPS and AEM measurements. Pressure ridges are not necessarily in isostatic equilibrium on a point-to-point basis and field observations indicate that the maximum keel depth is typically 3-5.5 times greater than the sail height (e.g., Melling and others, 1993, Bowen & Topham, 1996). Ridge-

specific values of ρ^* are therefore necessary to avoid overestimation of the thickness of ridges from IPS draft measurements. At the same time, the AEM data may also over estimate the thickness of deformed ice by assuming uniform ice conductivity and neglecting voids below the waterline that may interact with the secondary field (Reid and others, 2003, Pfaffling and others, 2007). With the thickness of pressure ridges gaining greater attention, primarily due to the hazard they pose to maritime operations, reducing these uncertainties will become increasingly important. Comparisons between coincident airborne and submarine measurements of ice thickness, in particular with the inclusion of accurate altimetry from an EM-bird, will likely be great value in constraining more sophisticated models for treating deformed ice. This underscores the importance of coordinated observing networks such as SIZONet.

Through direct comparison of coincident and colocated timeseries, we show that there is good agreement between ice velocities measured through acoustic bottom tracking with an upward-looking ADCP and those determined through optical flow analysis of imagery of the upper surface of the ice acquired by a coastal radar system (Figures 7 and 8). This is first independent validation of radar-derived ice velocities that we aware of and it demonstrates that surface radar can be an effective tool for quantitatively observing ice motion in the coastal zone. With the potential for greater temporal resolution, surface radar may provide a suitable alternative to bottom-moored ADCPs for measuring ice velocity in places where necessary infrastructure exists. Moreover, since they are able to provide data in real time, coastal radars represent an effective means of identifying certain ice-related hazards as they are happening and possibly before they occur.

Acknowledgements

This work was supported by the U.S. National Science Foundation (awards ARC 0632398 and 0856867), the U.S. Department of Homeland Security Center for Island Maritime and Extreme Environment Security (CIMES) and by a Grant in Aids for Scientific Research from the Japanese MEXT (awards 20221001 and 23654163). We also wish to thank the staff of CH2MHill Polar Services, the Barrow Arctic Science Consortium and UMIAQ for their field support in Barrow. We are also grateful to the North Slope Borough Department of Wildlife Management for use of their boat and assistance from their staff.

References cited

Arctic Council 2009. *Arctic Marine Shipping Assessment 2009 Report.* Arctic Council.

Belliveau, D.J., G.L. Bugden, B.M. Eid and C.J. Calnan 1990. Sea Ice Velocity Measurements by Upward-Looking Doppler Current Profilers. *Journal of Atmospheric and Oceanic Technology*, **7**(4): 596-602.

Bowen, R.G. and D.R. Topham 1996. A study of the morphology of a discontinuous section of a first year arctic pressure ridge. *Cold Regions Science and Technology*, **24**(1): 83-100.

Druckenmiller, M.L., H. Eicken, J.C. George and L. Brower 2010. Assessing the Shorefast Ice: Iñupiat Whaling Trails off Barrow, Alaska. In Krupnik, I., C.

469 Aporta, S. Gearheard, G.J.J. Laidler and L.K. Kielsen Holm, *eds. SIKU: Knowing*
470 *Our Ice*, Springer Netherlands, 203-228.
471 Druckenmiller, M.L., H. Eicken, M.A. Johnson, D.J. Pringle and C.C. Williams 2009.
472 Toward an integrated coastal sea-ice observatory: System components and a
473 case study at Barrow, Alaska. *Cold Regions Science and Technology*, **56**(2-3):
474 61-72.
475 Eicken, H., L. Shapiro, A. Gaylord, A. Mahoney and P. Cotter 2006. *Mapping and*
476 *characterization of recurring spring leads and landfast ice in the Beaufort and*
477 *Chukchi Seas.* Fairbanks, Final Report, Minerals Management Service, OCS
478 Study MMS 2005-068, Geophysical Institute, University of Alaska Fairbanks.
479 Fowler, C. 2003. Polar Pathfinder Daily 25 km EASE-Grid Sea Ice Motion Vectors.
480 [2003-2012]. NASA DAAC at the National Snow and Ice Data Center. .
481 Fukamachi, Y., G. Mizuta, K.I. Ohshima, T. Toyota, N. Kimura and M. Wakatsuchi
482 2006. Sea ice thickness in the southwestern Sea of Okhotsk revealed by a
483 moored ice-profiling sonar. *Journal of Geophysical Research-Oceans*, **111**(C9).
484 George, J.C., H.P. Huntington, K. Brewster, H. Eicken, D.W. Norton and R. Glenn 2004.
485 Observations on Shorefast Ice Dynamics in Arctic Alaska and the Responses
486 of the Iñupiat Hunting Community. *Arctic*, **57**(4): 363-374.
487 Gordon, R.L. 1996. Acoustic Doppler Current Profiler: Principles of Operation, A
488 Practical Primer. RD Instruments.
489 Haas, C., S. Hendricks, H. Eicken and A. Herber 2010. Synoptic airborne thickness
490 surveys reveal state of Arctic sea ice cover. *Geophys. Res. Lett.*, **37**(9): L09501.
491 Haas, C., J. Lobach, S. Hendricks, L. Rabenstein and A. Pfaffling 2009. Helicopter-
492 borne measurements of sea ice thickness, using a small and lightweight,
493 digital EM system. *J. Appl. Geophys.*, **67**(3): 234-241.
494 ISO 2010. International Standard ISO/DIS 19906: Petroleum and natural gas
495 industries – Arctic offshore structures. International Organization for
496 Standardization, 1,ch. De la Voie-Creuse, CP 56, CH-1211 Geneva 20,
497 Switzerland.
498 Jones, J. 2013. Landfast sea ice formation and deformation rear Barrow, Alaska:
499 Variability and implications for ice stability. (Master of Science University of
500 Alaska Fairbanks.)
501 Kurtz, N.T., T. Markus, D.J. Cavalieri, L.C. Sparling, W.B. Krabill, A.J. Gasiewski and J.G.
502 Sonntag 2009. Estimation of sea ice thickness distributions through the
503 combination of snow depth and satellite laser altimetry data. *Journal of*
504 *Geophysical Research-Oceans*, **114**.
505 Kwok, R. and G.F. Cunningham 2003. Sub-daily sea ice motion and deformation from
506 RADARSAT observations. *Geophys. Res. Lett.*, **30**(23).
507 Kwok, R. and G.F. Cunningham 2008. ICESat over Arctic sea ice: Estimation of snow
508 depth and ice thickness. *Journal of Geophysical Research-Oceans*, **113**(C8).
509 Laxon, S.W., K.A. Giles, A.L. Ridout, D.J. Wingham, R. Willatt, R. Cullen, R. Kwok, A.
510 Schweiger, J. Zhang, C. Haas, S. Hendricks, R. Krishfield, N. Kurtz, S. Farrell
511 and M. Davidson 2013. CryoSat-2 estimates of Arctic sea ice thickness and
512 volume. *Geophysical Research Letters*, **40**(4): 732-737.

513 Mahoney, A.R., H. Eicken and L. Shapiro 2007. How fast is landfast sea ice? A study of
514 the attachment and detachment of nearshore ice at Barrow, Alaska. *Cold*
515 *Regions Science and Technology*, **47**(3): 233-255.
516 Mahoney, A.R., H. Eicken, L.H. Shapiro, R. Gens, T. Heinrichs, F.J. Meyer and A.
517 Gaylord 2012. Mapping and Characterization of Recurring Spring Leads and
518 Landfast Ice in the Beaufort and Chukchi Seas. OCS Study BOEM 2012-067.
519 Melling, H., P.H. Johnston and D.A. Riedel 1995. Measurements of the Underside
520 Topography of Sea Ice by Moored Subsea Sonar. *J. Atmosph. Ocean Technol.*,
521 **12**: 589-602.
522 Melling, H., D.R. Topham and D. Riedel 1993. Topography of the upper lower
523 surfaces of 10 hectares of deformed sea ice. *Cold Reg. Sci. Technol.*, **21**: 349-
524 369.
525 Mv, R., J. Jones, H. Eicken and C. Kambhamettu 2013. Extracting Quantitative
526 Information on Coastal Ice Dynamics and Ice Hazard Events From Marine
527 Radar Digital Imagery. *Geoscience and Remote Sensing, IEEE Transactions on*,
528 **51**(5): 2556-2570.
529 Pfaffling, A., C. Haas and J.E. Reid 2007. Direct helicopter EM - Sea-ice thickness
530 inversion assessed with synthetic and field data. *Geophysics*, **72**(4): F127-
531 F137.
532 Reid, J.E., A.P. Worby, J. Vrbancich and A.I.S. Munro 2003. Shipborne electromagnetic
533 measurements of Antarctic sea-ice thickness. *Geophysics*, **68**(5): 1537-1546.
534 Schmidt, C. 2011. Despite Data Gaps, US Moves Closer to Drilling in Arctic Ocean.
535 *Science*, **333**(6044): 812-813.
536 Shapiro, L.H. and R. Metzner 1989. Nearshore ice conditions from radar data, Point
537 Barrow, Alaska. Geophysical Institute, University of Alaska Fairbanks UAG R-
538 268.
539 Stroeve, J., M. Serreze, M. Holland, J. Kay, J. Malanik and A. Barrett 2012. The Arctic's
540 rapidly shrinking sea ice cover: a research synthesis. *Climatic Change*,
541 **110**(3): 1005-1027.
542 Thorndike, A.S., D.A. Rothrock, G.A. Maykut and R. Colony 1975. The thickness
543 distribution of sea ice. *J. Geophys. Res.*, **80**: 4501-4513.
544 Timco, G.W. and R.M.W. Frederking 1996. A review of sea ice density. *Cold Reg. Sci.*
545 *Technol.*, **24**: 1-6.
546 Wang, M.Y. and J.E. Overland 2012. A sea ice free summer Arctic within 30 years: An
547 update from CMIP5 models. *Geophysical Research Letters*, **39**.
548 Warren, S.G., I.G. Rigor, N. Untersteiner, V.F. Radionov, N.N. Bryazgin, Y.I.
549 Aleksandrov and R. Colony 1999. Snow depth on Arctic sea ice. *J. Climate*, (6):
550 1814-1829.
551 Williams, S.B., O. Pizarro, M. Johnson-Roberson, I. Mahon, J. Webster, R. Beaman and
552 T. Bridge 2008. AUV-assisted surveying of relic reef sites. *OCEANS 2008*, 1-7.
553
554